

MICROROBOTIC LASER STEERING FOR MINIMALLY INVASIVE SURGERY[†]

Peter A. York^{1,2*}, Rut Peña^{1,2}, Daniel Kent^{2,3}, and Robert J. Wood^{1,2}

¹John A. Paulson School of Engineering and Applied Sciences, Harvard University, 60 Oxford St, Cambridge, MA

²Wyss Institute for Biologically Inspired Engineering, 3 Blackfan Circle, Boston, MA

³Beth Israel Deaconess Medical Center, 110 Francis St, Boston, MA

*To whom correspondence should be addressed: pyork@g.harvard.edu

The creation of multi-articulated mechanisms for use with minimally invasive surgical tools is difficult due to fabrication, assembly, and actuation challenges on the millimeter scale of these devices. Nevertheless, such mechanisms are desirable for granting surgeons greater precision and dexterity to manipulate and visualize tissue at the surgical site. Here, we describe the construction of a complex opto-electro-mechanical device that can be integrated with existing surgical tools to control the position of a fiber-delivered laser. By using modular assembly and a laminate fabrication method, we are able to create a smaller and higher bandwidth device than the current state of the art while achieving a range of motion similar to existing tools. The device we present is 6 millimeter in diameter and 16 millimeter in length and is capable of focusing and steering a fiber-delivered laser beam at high speed (1.2 kilohertz bandwidth) over a large range (over ± 10 degree in both of two axes) with excellent static repeatability (200 micrometer).

Summary

Advances in microrobotic design, fabrication, and control enable the dexterous control of a laser in a millimeter-sized package.

[†] This manuscript has been accepted for publication in Science Robotics. This version has not undergone final editing. Please refer to the complete version of record at robotics.sciencemag.org/content/6/50/eabd5476. The manuscript may not be reproduced or used in any manner that does not fall within the fair use provisions of the Copyright Act without the prior, written permission of AAAS.

Introduction

In minimally invasive surgery, access is gained to internal anatomy through natural orifices or small external incisions. It encompasses diverse practices such as the catheter delivery of stents, flexible endoscopy of the gastrointestinal tract, laparoscopic treatment of abdominal diseases, and transnasal operation at the skull base for neurological conditions. Common to many of these procedures is the need for wristed articulation at the distal ends of tools for manipulating tissue and visualizing the surgical site (1). This was an important motivation for introducing robotics into minimally invasive surgery (2) and remains a vibrant area of research and development today (3–5).

This work addresses this large challenge by focusing on a subset of the tools used in minimally invasive surgery: those used for energy delivery. Common surgical energy sources include monopolar and bipolar radio frequency electric current (electrosurgery), thermal cautery (direct current heating), ultrasonic vibrations, argon beam coagulation (argon assists the conduction of radio frequency current), and lasers (6). These tools are essential to the surgical workflow because they enable the cutting, coagulation, and desiccation of tissue deep inside the body. The different energy sources ultimately have the same effect: denaturizing proteins through the heating of tissue. Moreover, they are at present used in a similar way: brought close (a few millimeters) to the tissue, and energy is delivered directly from the electrode or fiber to the anatomy.

However, a more sophisticated approach is possible when it comes to delivering laser energy. Though current laser-based tools are used in the static, close-contact way (7–10), a robotic approach could be employed to steer the laser. Because lasers can be focused and steered using low-inertia optical components, high-bandwidth distal actuation can be used to control the laser position. This would yield the same benefits that robotic wrists grant to mechanical end effectors (i.e., the ability to work around corners and navigate obstacles) while achieving additional capability to precisely control the speed of the laser on the tissue over a wide range. This is important because laser speed strongly affects the duration of laser irradiation, a critical determinant of the quality of laser/tissue interaction: incision depth, spread of thermal damage, and hemostatic effect (11–13).

The improved incision quality possible with robotic laser steering is demonstrated by Remacle, et al (14), who use an external laser manipulator to achieve delicate resections of vocal fold lesions. This system relies on a line-of-sight pathway through the airway, which limits its use in other surgical arenas. However, its capabilities provide a reasonable initial set of performance goals for an endoscopic laser steering system. It uses laser speeds of 29 mm/s and typical incision lengths of 0.5 to 3.5 mm (15). A range of motion larger than typical incision length is likely desirable for minimizing the repositioning needed of the fiber-delivery device. Similarly, increased laser speed is desirable for enabling operation with a wide variety of surgical lasers; appropriate laser speed increases with increased laser pulse frequency and laser spot size, assuming similar overlap between pulses is desired.

The challenge to creating this type of robotic device is the opto-electrical-mechanical complexity needed in a small package. Device diameter is the key constraint and depends on the type of surgical tool being used; a sampling of commonly used tools shows a range of different sizes: colonoscopes ranging from 9.7 to 14.8 mm (PCF-PH190I/L and CF-FH260AZI/L, Olympus Medical Systems), laparoscopic tools either 5 or 8 mm (da Vinci SP, Intuitive Surgical), rhinolaryngoscopes for transnasal access ranging from 2.6 to 4.9 mm (ENF-V3 and ENF-VT3,

Olympus Medical Systems), and cardiac catheters ranging from 2.67 to 3.33 mm, (AcuNav, Biosense Webster).

Several research groups have proposed solutions to the robotic laser steering problem, yielding two broad approaches, summarized in Table 1. In both, a flexible optical fiber delivers a laser to the end effector of a minimally invasive surgical tool. In the first approach, which we term “fiber steering”, the tip of the fiber is robotically bent to control the spot position on the surgical site. This is the approach of Kundrat, et al., (16, 17), who embed the laser fiber inside a two-segment continuum manipulator driven by push-pull rods. Similarly, Zhao, et al., (18) use cables as mechanical transmissions to bend the distal tip of the optical fiber. The strength of these methods is their simplicity: they do not require complex manufacturing of miniature actuators or sensors; moreover, they achieve large ranges of motion (45×45 mm and 28 mm diameter, respectively). However, laser speed is limited (3 mm/s and 3.5 mm/s) by the use of cables and rods. Acemoglu, et al., (19) strike a different balance. They use miniature electromagnetic coils to bend the fiber via a permanent magnet that is bonded to the fiber. They achieve a larger laser speed (94 mm/s), but because of pernicious trade-offs related to the size of the coils and permanent magnet, the range of motion is reduced to 4×4 mm – five to ten times less than the cable and rod driven devices.

In the second approach, called “optical steering”, mirrors and/or prisms are used to control the laser spot position after it exits the flexible optical fiber. This approach was taken by Andreff, et al., (20, 21) who used linear piezoelectric motors to control the angle of a flexure-supported tip-tilt mirror. They achieve a moderate speed (33 mm/s) and range of motion (20×20 mm), but the optical configuration requires the use of an unwieldy external mirror that occludes the field of view and makes integration with focusing optics difficult. Patel, et al., (22) provide a different approach, in which they use miniature piezoelectric motors to rotate Risley prisms. They achieve a greater maximum speed (167 mm/s) with similar range of motion (26.5 mm diameter). However, their use of rotary transmission elements makes further miniaturization challenging from the demonstrated diametral size of 17 mm.

We herein describe our advancements in design, fabrication, and control that allow us to surpass the performance of the state-of-the-art in terms of miniaturization (6 mm diameter) and laser speed (3900 mm/s), while achieving a similar range of motion (18×18 mm). Our approach, summarized in Movie 1, builds on the preliminary work shown in (23), in which we showed that piezoelectric bending actuators can be used in conjunction with miniature compliant mechanisms to generate the rotations of miniature mirrors in a compact package. In this work, we first lay out general design principles for building miniature laser galvanometers and develop the key insight that the use of three mirrors counterintuitively allows greater miniaturization than two mirrors. This follows from ray tracing of the laser trajectory inside the galvanometer. Secondly, we employ a modular fabrication technique in which individual components are placed on disks and assembled on a railed superstructure. This simplifies the typically challenging problem of assembling complex millimeter-scale systems and enables us to achieve a rich feature density. It also allows the device to be easily assembled and disassembled, which allows for rapid testing, debugging, and development. We also leverage printed circuit MEMS techniques (PC-MEMS) for making miniature compliant mechanisms that allow us to generate large-angle mirror rotations without sacrificing miniaturization (24, 25). Lastly, for control, we implement a low-dimensional hysteresis compensation scheme that corrects for the hysteresis in the piezoelectric bending actuators and intermediate mechanisms. In this work, we validate our microrobotic approach to laser steering using a low powered visible laser, which facilitates testing and development, with the vision of integrating with surgical lasers in future work.

Of these contributions, the fabrication advancements will be most broadly useful within the robotics field. The problem of simple, repeatable device assembly is a bottleneck in the development of complex microrobotic devices, which we surmount using the disk-and-rail modular assembly technique. This method can be employed and adapted for the construction of complex microrobotic devices, both within and outside of the medical robotics context. The design and control advancements are also important, but their impact will likely be more limited to the development of laser-based and/or piezoelectric-based microrobotic devices.

Results

Our microrobotic laser steering device is 6 mm in diameter and can thus be seamlessly integrated into existing workflows in flexible gastroenterology and single-port surgery – settings in which adapting traditional tools is difficult and lasers are of particular interest (26). The laser steering tool is shown as a standalone device in Fig. 1A and integrated with a colonoscope (Olympus CF-100L) in Fig. 1B-C. It is shown external to the colonoscope but it is small enough to be internally integrated into a special-purpose flexible scope. The device is 16 mm in length and possesses the ability to steer a focused laser beam through over $\pm 10^\circ$ on two orthogonal axes with a 1.2 kHz mechanical bandwidth. Its principle of operation, demonstrated in Movie S1, is as follows: a gradient-index collimating lens collects light from a ferrule-terminated optical fiber and directs it into a miniature plano-convex focusing lens. The light is reflected by a 45° angle-of-incidence mirror and into a miniature two-mirror galvanometer. Flexible linkages convert the quasi-linear motion of piezoelectric bending actuators into the rotational motions of the galvanometer mirrors.

In this section, we describe the design, fabrication, and control insights that culminate in our laser steering solution. We first describe general design considerations for miniaturizing the galvanometer portion of the device. This is the least straightforward component to miniaturize both in terms of design and fabrication. Next, we present details for the design and construction of each component and the assembly thereof. Third, we report the methods used for static position control and characterization. Last, we describe the dynamic properties of the device, demonstrate the ability for high-bandwidth operation, and interface the device with a commercial colonoscope.

General design considerations For the galvanometer design, the objective is to minimize the distance between the mirrors, given the beam size, mirror size, and desired range of motion, all while avoiding collisions between the mirrors and between the reflected beam and previous mirrors in the optical path (Fig. 2). An important high-level design consideration is the number of mirrors used. Somewhat counterintuitively, a three-mirror design can actually be made smaller than a two-mirror design, if the same range of motion is desired for each.

To see this is the case, consider the three mirror design shown in Fig. 2A: if the distance between the first and second mirrors is too small, then the reflected beam from the third mirror will intersect the first mirror. If the distance between the second and third mirrors is too small, then those mirrors will collide. However, increasing the distance between mirrors not only increases device size, but it also means that larger area mirrors are needed to collect the reflected light for the same range of motion. The three-mirror design shown balances all of these considerations to yield a device with $\pm 10^\circ$ range of motion on each active mirror in a 4 mm diameter footprint. Note that the use of chamfered corners on the mirrors increases the range of motion by preventing collisions in critical locations.

The first two-mirror design (Fig. 2B) has the same diametral footprint as the three-mirror design but its range of motion is halved on the first mirror axis. The loss in range of motion follows from an unfortunate set of tradeoffs. If the mirrors are too close together, then the beam

reflected from the second mirror will intersect the first mirror for large positive rotation angles of the first mirror. On the other hand, if the distance between the two mirrors is increased, then the second mirror must be enlarged to accept the incident light for large negative rotation angles of the first mirror. This is the second two-mirror design (Fig. 2C); it achieves the same range of motion as the three-mirror design (Fig. 2A) at the expense of a 50 % increase in diameter.

Throughout this analysis we assumed a collimated beam diameter of 1 mm. This is larger than the low-power pointing laser used herein for device validation, but it is a reasonable choice for a collimated high-power beam. For simplicity, we also chose the neutral position of each mirror to be at 45° angle of incidence with the incoming beam; allowing this to slightly deviate from 45° might yield slightly different results but would not change the structure of the design trade-offs. We also assumed that a symmetric range of motion is desired. Once again, if this was not the case, then the resulting design might change slightly, but the nature of the design space would not change. Lastly, it should be emphasized that we have been considering the case of the exiting ray being parallel to the incoming fiber (forward looking, per (27)). If we wanted the exiting ray to be perpendicular to the incoming fiber (side looking), there would be no reason to use a three-mirror design; a two-mirror design would be perfectly acceptable in terms of miniaturization and range of motion. However, because most energy delivery tools used in surgery are forward-looking, we chose to use that configuration for our device.

Another small point of differentiation between the three and two-mirror designs for the forward looking configuration is the shape of the focal plane. Because the distance the laser travels through the three-mirror design changes very little as mirror angles change, the focal plane is nearly symmetric about the neutral configuration. This is not the case for the two-mirror designs; the distance the laser travels between the mirrors changes drastically with changing mirror angles. This yields the deformed focal plane that is contracted for large negative values of the first mirror rotation angle, as seen in the previous version of this device (23).

Detailed design and fabrication With those general insights in hand, we undertake the detailed design and fabrication of the device. For fabrication, we use a mixture of off-the-shelf components and custom-made parts that are primarily created using laser micromachining (Oxford Lasers E Series with Coherent Avia 355-7 laser). The assembled three-mirror galvanometer is shown in Fig. 3A, and each component before assembly is shown in Fig. 4. The assembly process is shown in full in Movie S2. Specific details for component design, fabrication, and function are as follows:

1. **Steel-rod superstructure.** This component consists of two 500 μm and one 300 μm diameter stainless steel rods (Misumi USA) onto which the remaining components are assembled. The rods are orthogonally located into a FR4 disk using an alignment jig. A spring steel preload spring to compress and hold the assembled components in place is attached to the disk. All components were laser micromachined.
2. **Ferruled fiber and collimating lens.** An off-the-shelf ferrule terminated optical fiber (SMP- F0106-FC, Thor Labs, Inc., NJ) was assembled with a gradient index collimator (GRIN2306A, Thor Labs, Inc., NJ) and attached to an FR4 support disk.
3. **Piezoelectric bending actuators.** These were made to size using the process and materials described in (28). We chose actuator dimensions in accordance with the available space adjacent to the optical components: active length of 7 mm, tip length of 1.8 mm, bridge length of 0.5 mm, base width of 1.4 mm, and tip width of 0.4 mm. The actuators are driven in the biased unipolar configuration with a fixed bias voltage,

so each is controlled by a single time-varying input signal ranging from zero to the bias voltage. To achieve a sizeable output displacement while ensuring that the tensile strain in the piezoceramic is well below the failure limit, we chose a fixed bias voltage of 200 V. Under that drive condition, the actuators achieve free displacement of $\pm 200 \mu\text{m}$ and have a first resonant frequency of 2.6 kHz.

4. **Focusing lens.** This was acquired as an off-the-shelf component (#89-003, Edmund Optics) and ground down to size using an alignment jig and a diamond cut-off wheel. Registration marks laser pre-engraved into the lens allow alignment of the optical center after grinding.
- 5, 6. **Articulate mirrors and motion transmissions.** These are complex assemblies of rigid and flexible components fabricated using PC-MEMS. They consist of four-bar crank-slider linkages formed from stainless steel, polyimide, and a heat-curable acrylic adhesive (Pyralux FR1500, Dupont Inc., Wilmington, DE). The mirrors are located on the cranks and the sliders each interface with one of the piezoceramic actuators, as shown schematically in Fig. 3B. The x-axis transmission additionally contains a linearizing linkage to compensate for the out-of-plane motion of the bending actuator tip. The mirrors are made from sputtered aluminum (Denton Desktop Pro PVD system, Denton Vacuum LLC, Moorestown, NJ) on a $100 \mu\text{m}$ fused silica substrate and singulated using an ultraviolet laser.

The detailed design of the transmissions follows from the actuator properties. We wanted to achieve at least $\pm 10^\circ$ of motion for each mirror, in accordance with the state-of-the-art. To achieve this in our device there are two important design considerations: (1) the transmission ratios of the linkages and (2) the stiffnesses of the linkages relative to that of the actuators. Based on experience sizing similar mechanical components (29), we chose a target transmission ratio of $0.1^\circ/\mu\text{m}$ and target stiffness equal to that of the actuators. In the device, we achieved transmission ratios of $0.13^\circ/\mu\text{m}$ and $0.12^\circ/\mu\text{m}$ (due to small fabrication errors) and stiffnesses of 60% and 90% the actuator stiffness, respectively, as can be seen in the experimental data (Fig. 3C). Note that the stiffness of the transmission is in parallel to the actuator stiffness and results in reduction of the free displacement of the actuators. Thus fabricated, we achieve ranges of motion 12.5 to 20° and 11.2 to 13.7° for the two mirrors, respectively. The asymmetry corresponds to small assembly misalignment and slightly nonlinear transmission kinematics. The neutral (zero) mirror angles and actuator positions correspond to the configuration for which the output beam is aligned along the longitudinal axis of the device.

7. **Fixed mirror.** This aluminum-sputtered fused silica mirror is fixed at 45° relative to the incident light using two alignment blocks that in turn interface with an FR4 support disk.
8. **Retaining clip.** This spring steel component fits onto grooves rastered into the stainless steel rods of the superstructure. It axially constrains the assembly in conjunction with the preload spring located on the superstructure base.
9. **Spacer tubes and disks.** These pieces are laser micromachined to ensure proper spacing and alignment between components. Tube length and disk thickness are the critical dimensions.

Position control and characterization We began characterizing the device by measuring open loop repeatability, which is an important metric because it describes the fundamental limitations of the device physics to reproduce identical motions. Stiction, plasticity, and other phenomenon mean that identical inputs do not produce identical outputs. Unidirectional repeatability is a measure of repeatability in which measurement points are only approached from one direction. Measurement results for unidirectional repeatability are shown in Fig. 5A. The maximum 2σ standard distance of the sampled points is $200\ \mu\text{m}$, which means that there is 95% confidence that any series of identical movements will fall within a $200\ \mu\text{m}$ radius of dispersion about the mean trajectory.

The presence of hysteresis complicates position control. Hysteresis is a bidirectional effect that arises primarily from domain reorientation inside the piezoceramic actuator; it means that the laser position depends on the time history of the input. This is clearly undesirable because it complicates control and makes use of the device unintuitive. To minimize the hysteretic effects, we implemented a feed forward compensation scheme, which is described in detail in the Materials and Methods. To validate our approach, we commanded the star trajectories shown in Fig. 5B-C and Movie S3 for uncompensated and compensated inputs. The raw inputs clearly show the effects of path dependence, while the corrected inputs show improved tracking; this is, essentially, a measure of bi-directional repeatability. Quantitatively, we find that the maximum 2σ standard distance around the setpoints is $2.14\ \text{mm}$ without compensation and $0.72\ \text{mm}$ with compensation. This is reasonable improvement for feed forward compensation; further improvement can be achieved with feedback control.

Because of the low dimensionality of the workspace and input space and the lack of sensor information, we chose to control the device using a direct model-free mapping between actuator input and laser spot position, cascaded with the feed forward compensation for hysteresis. We fit third and second degree polynomial surfaces to the open loop repeatability measurement data for the first and second mirrors, respectively. These fits were centered around $73\ \text{V}$ and $93\ \text{V}$ for the x and y-axis actuators, respectively, which correspond to neutral angles of the mirrors. The size of the “calibrated workspace” formed in this way was $18 \times 18\ \text{mm}$, which is slightly smaller than the approximately $22 \times 22\ \text{mm}$ uncalibrated workspace shown in Fig. 5A.

Dynamic control and characterization The bandwidth of the system is limited by resonant oscillation of the mirrors at high frequencies. The primary resonant frequencies for the two mirrors are $1.8\ \text{kHz}$ and $1.9\ \text{kHz}$, as can be seen in the Bode plots shown in Fig. 6A-B. Additionally, there is a lower frequency mode at $1.2\ \text{kHz}$ on the first mirror (likely due to twisting or another off-axis mode). To avoid exciting these modes, we use a finite jerk motion profiling scheme (also known as sigmoid or S profiling) as seen in Movie S4. The time histories of those trajectories are shown in Fig. S4.

The system shows only minor deviation from static trajectories at high speeds, as can be seen in Fig. 6C-D and Movie S5. There is only 5% deviation between the trajectories followed at low ($7.8\ \text{mm/s}$) and high ($3900\ \text{mm/s}$) speeds. Also, because of the two-axis control, the system can trace complex planar trajectories, as shown in Fig. 6E-F and Movie S6. The large bandwidth in the system can also be exploited to generate multi-modal profiles, as seen in Movie S7. These are trajectories in which a high frequency input is superimposed onto a low frequency one. This allows the user to change the effective laser spot size on the fly, which is particularly relevant for situations in which a large area needs to be controllably covered, as in large-area hemostasis.

Colonoscope interfacing Because of the low-profile and small mass of the laser steering device ($717\ \text{mg}$), it can be readily interfaced with existing surgical tools. To demonstrate this, we

attached it onto the end of a colonoscope (Olympus CF-100L) and performed a simulated polyp resection task on a benchtop surgical simulator, which can be seen in Fig. 1C and Movie S8. We demonstrate both teleoperated control using a standard input device (Phantom Omni, Sensable Technologies) and robotic high-speed control of the laser along a registered incision trajectory. The system architecture and mapping used for teleoperation are described in the Materials and Methods.

Discussion

In this work we describe microrobotic advances that point the way forward to new methods of controlling lasers in minimally invasive surgery. Ultimately, we anticipate that giving surgeons greater control over laser speed when interacting with tissue will enable the quality of laser/tissue interactions to be more widely tuned and optimized than possible with existing statically wielded tools. We also expect that robotic steering of lasers will improve access to areas difficult to reach with rigid tools. Lastly, we envisage that the use of steerable, focused lasers will allow energy to be delivered to tissue without occluding the surgeon's field of view. These are the ultimate aims toward which this work represents an important milestone.

Several technical challenges remain, primary of which is the incorporation of high-powered surgical lasers and suitable optical components. The choice of optical materials depends on the wavelength and power of the laser being used. For example, if a CO₂ laser is being used, gold-sputtered aluminum mirrors and Zinc Selenide lenses provide appropriate reflectance and transmission, respectively. Particular attention must be paid to the "laser-induced damage threshold," which is a measure of the laser power that an optical component can experience before degradation. Details for the scaling of the optical components when used with a particular surgical laser are given in the Supplementary Materials.

Regardless of the laser modality used, the device will need to be encapsulated so as to be robust to the fluids and debris in the surgical environment and allow for sterilization. Cleaning and safety protocols will need to be developed. Because the tips of laser fibers can be damaged after extended use, it may be advantageous to incorporate a method for decoupling the laser fiber from the device. This would allow the independent cleaning and cleaving of the laser fiber, which can expand its lifetime (30).

Conversely, it may be desirable to directly embed the device into a flexible endoscope. This would simplify the encapsulation and robustness challenges and prevent the device from partially occluding the scope's field of view. The downside of this approach would likely be an increase in cost as a dedicated endoscope would be needed instead of an add-on to existing endoscopes. Kiesslich, et al. demonstrate this integrated approach with a similar device by embedding a 5 mm diameter, 43 mm long confocal microscope into a standard flexible colonoscope (31). Our device is slightly larger in diameter and shorter in length than theirs, but it is similar enough in size to be similarly deployed.

The lack of intrinsic tactile feedback is a limitation of non-contact energy delivery methods, including the laser based approach described here. To remedy this, several researchers have proposed haptic feedback schemes. Rizin, et al., (32) described the basic concept of generating a virtual surface corresponding to the surgical site and modulating the laser power based on the user's interactions with the virtual surface. In a more sophisticated scheme, Fischera, et al. (33), used an estimation of laser incision depth to generate haptic interaction for the user. Other researchers, including Olivieri, et al., (34) and Kundrat, et al., (16) have investigated generating active constraints along desired trajectories to help guide the user's movement. There

seems to be merit to each of these schemes, with the correct approach for a given task being application dependent. In laryngeal applications, in which retention of healthy tissue is critical, this might involve using active constraints to guide incisions away from healthy tissue, whereas in gastrointestinal applications, for which perforation of the bowels is a major complication, a haptic feedback scheme incorporating incision depth information may be preferable. This remains an important area for systematic exploration and technology development for laser based surgical tools.

To achieve accuracy in line with the repeatability of the device, sensory feedback will need to be incorporated. A simple approach would be to embed strain gauge sensors within the piezoelectric bending actuators (35) to estimate actuator position and to use current sensing to estimate actuator velocity (36). The mirror position could then be calculated from the transmission kinematics and the laser position estimated from the model of specular reflection described in our prior work (23). Measuring the mirror position directly would result in a better laser position estimate, but the pathway to a suitable miniature sensing method is not as straightforward as sensing the actuator motion. Alternatively, visual feedback could be used for high quality estimates, albeit with lower sample rates than achievable with electromechanical sensors. In practice, a sensor fusion that blends these different pieces of information is likely the best approach.

Our laser steering approach also may enable new approaches for endoscopic visualization and visual biopsy. In optical coherence tomography and confocal endomicroscopy, laser/tissue interactions are used to visualize subsurface structures, and scanning allows a large area of tissue to be seen at once. Optical steering can also be used to increase the effective field of view of standard white light imaging tools, through stitching together a set of images acquired through rapid scanning. The scanning system and modular device assembly approach we describe can be adapted to the fabrication of millimeter-sized versions of those systems. Even smaller versions of these systems are built using MEMS techniques (27) that use electrostatic and electothermal actuators to excite resonant scanning elements. Our approach does not supplant these MEMS devices when absolute miniaturization is desired, but it does present advantages in terms of simplicity of construction and the ability to achieve a large quasistatic range of motion.

We also anticipate that this technology can be adapted for use in other microrobotic systems, particularly in micro aerial vehicles and satellites for which size and weight are at a premium (29, 37). This technology will enable the fabrication of miniature light detection and ranging (LiDAR) sensors used for mapping and navigation (38), as well as laser scanners used for wide-area atmospheric sensing of pollution (39).

Materials and Methods

Hysteresis modeling and compensation

Because of hysteresis, actuator position is not a simple function of input voltage; rather it depends on input voltage, input voltage history, and the current sign of the input. This complicates the position control problem, but by modeling and understanding this relationship, we can largely remove the hysteretic effects through inverting the hysteresis model and using it as a feed forward control term. We began by capturing displacement response data for an unloaded bimorph actuator for two amplitude rich input conditions, shown in Fig. 7A-B. This is a standard approach for capturing the effects of hysteresis throughout the input space. We then mapped the displacement data to the same range as the input space and inverted the relationship, yielding the

curves shown in shown in Fig. 7C-D. These are the curves to parameterize and use in feed forward control.

We undertake this parameterization using a modified version of the polynomial basis function approach described in (40). Our approach is to use two families of quadratic weighted sine functions, one for the positive-going curves and one for the negative-going curves. Implementation is as follows, using Fig. 7E as a visual guide. The outer curves f_p and f_n that form the hysteretic envelope are defined as:

$$f_p(V) = V_{max} \left(a_p (V - h_p)^2 + k_p \right) \sin(\pi V / 2V_{max})$$

$$f_n(V) = V_{max} + V_{max} (a_n (V - h_n)^2 + k_n) \sin(\pi (V - V_{max}) / 2V_{max})$$

where V_{max} is the maximum excursion of the input voltage. With these expressions, we first need to ensure that f_p and f_n are equal at the minimum and maximum excursions of the input voltage. We already have that $f_p(0) = 0$ and $f_n(V_{max}) = V_{max}$, but we also want to ensure that $f_p(V_{max}) = V_{max}$ and $f_n(0) = 0$. This leads to the choices of:

$$a_p = \frac{1 - k_p}{(V_{max} - h_p)^2} \quad a_n = \frac{1 - k_n}{h_n^2}$$

Note that k_p and k_n control the size of the hysteresis loops and h_p and h_n control the shape. In anticipation of scaling these curves to the interior of the hysteretic envelope, we rescale h_p and h_n using the relations:

$$h_p = l_p V_{max} \quad h_n = l_n V_{max}$$

Thus, the parameters k_p , k_n , l_p , and l_n fully define the shape of f_p and f_n , for a chosen value of V_{max} .

Now, the positive-going family of curves g_p and negative-going family of curves g_n can be defined as follows:

$$g_p(V, V_L) = f_n(V_L) + V_{amp} \left(a_p (V - h_p)^2 + k_p \right) \sin(\pi (V - V_L) / T)$$

$$g_n(V, V_U) = f_p(V_U) + V_{amp} (a_p (V - h_n)^2 + k_n) \sin(\pi (V - V_U) / T)$$

where V_L and V_U parameterize the curve families and V remains the independent variable. As seen in Fig. 7E, V_L denotes the point at which g_p intersects f_n , and V_U denotes the point at which g_n intersects f_p . Now, in order to make sure that each family of curves scales appropriately in size and shape, we have the constraints for the g_p family of curves:

$$V_{amp} = V_{max} - f_n(V_L) \quad T = 2(V_{max} - V_L)$$

$$h_p = l_p V_{max} + (1 - l_p) V_L \quad a_p = \frac{(1 - k_p)}{(V_{max} - h_p)^2}$$

Similarly, for the g_n family of curves we choose:

$$V_{amp} = f_p(V_U) \quad T = 2V_U$$

$$h_p = l_n V_U \quad a_p = \frac{(1 - k_n)}{h_n^2}$$

With these constraints, the parameters k_p , k_n , l_p , and l_n fully define g_p and g_n for some value of V_{max} .

The curves g_p and g_n are then used to calculate the corrected input from some nominal input. The current value of V_L or V_U denotes which member of g_p or g_n the system is operating on, and when the sign changes, the first step is to look for a new V_L or V_U . The transition point at which this occurs is denoted V_T , and to determine which new curve to transition onto, one solves the nonlinear root-finding problem:

$$g_p(V_T, V_L) - g_n(V_T, V_U) = 0$$

for the unknown variable (either V_L or V_U). With this in hand, one can calculate the desired feed-forward correction factor (g_p or g_n) for the current nominal input voltage. The process of finding the corrected input for a given nominal input is shown for a sample trajectory in Fig. 7E.

Using this approach, the measured curves are fit to the parameters: ($k_p = 0.81$, $l_p = 0.5$, $k_n = 0.80$, and $l_n = 0.53$), as shown in Fig. 7C-D. In practice, the loading from the hinged transmissions slightly deforms these curves; for in situ hysteresis compensation, we used a tuned set of parameters ($k_p = 0.82$, $l_p = 0.5$, $k_n = 0.75$, and $l_n = 0.608$). Lastly, note that this is a quasistatic approach; piezoelectric hysteresis has some rate dependence, but we found the simple rate independent approach to be sufficient for this application and the range of frequencies used.

Experimental setup and procedures

Laser position measurements Laser position data was collected using a calibrated high-speed camera (Phantom v710, Vision Research, Inc., Wayne, NJ) at 1200×800 pixel resolution with a Nikon AF Micro-Nikkor 200 mm f/4D IF-ED macro lens. The camera has a maximum frame rate of 7500 frames per second at full resolution. Lighting was provided from two low-flicker LED lights (Zaila, Nila, Inc., Altadena, CA). This measurement setup is shown in Fig. S2A.

Reprojection errors from the calibration were less than 0.2 pixel ($10 \mu\text{m}$ at the chosen focal length). Sub-pixel reprojection error means that the camera calibration captures the physics of the measurement setup well and means that camera calibration is an only minor source of measurement error. Larger contributors are likely to be differences in lighting and marker detection. The measurement resolution in the camera orientation used for data collection was $46 \mu\text{m}/\text{pixel}$ and $51 \mu\text{m}/\text{pixel}$ in the world x and y directions, respectively.

Teleoperation architecture The teleoperation system maps the user's control of a joystick input device (Phantom Omni, Sensable Technologies) onto the motion of the laser. We use a clutching scheme, in which the system only registers the user's input if a button on the joystick is pressed. This allows the user to reposition their body on the fly to maintain a dexterous grasp of the input device. The pose of the input device is collected using the OpenHaptics API (3D Systems, Rock Hill, SC). During each software loop, the body frame difference (T_d) between current (T_c) and previous (T_p) input device poses is calculated according to:

$$T_d = T_p^{-1}T_c$$

where T_d , T_p , and T_c are members of $SE(3)$. The x and y components of the body linear velocity (v_x and v_y) are then given by:

$$\begin{aligned} v_x &= T_{d,14}/\Delta t \\ v_y &= T_{d,24}/\Delta t \end{aligned}$$

where Δt is the loop time. These components are used because they point orthogonal to the joystick body and thus provide a natural basis for the laser control. This desired laser velocity is sent to a computer running a real time operating system (XPC Target, MathWorks, Natick, MA) that scales the desired velocity and integrates to generate a desired position, which is then mapped to control voltages using the calibration and feed forward mapping. Lastly, the control voltages are amplified using a piezoelectric amplifier (Trek PZD 350A, Advanced Energy Industries, Inc., Denver, CO). The system architecture is illustrated graphically in Fig. S2B-C.

Kinematics We measured the relationship between actuator displacement and mirror angle for the entire input space in 20 V increments using a high zoom inspection camera (Pixel-link PL-B741F). The resolution of the measurement system was 2.5 $\mu\text{m}/\text{px}$.

Repeatability We undertook unidirectional repeatability measurements using the standard for single axis motion control systems (ISO 230-2). Under these guidelines, we measured 20 different points in the laser workspace 10 times each, for a total of 200 data points. For each measurement, the system was powered off and reset, so as to eliminate the influence of hysteretic effects. A typical data set of 20 points is shown in Fig. S3; this image contains all 20 sampled points superimposed onto a single image.

Bandwidth and actuator performance The frequency responses of the unloaded actuators and the full actuator/transmission/mirror subsystems were measured using a laser Doppler vibrometer (PSV-500, Polytec GmbH, Waldbronn, Germany). The static displacement and hysteresis characteristics of the bare actuators were measured using the same system.

List of Supplementary Materials

Fig. S1. Time history of step and sigmoid responses

Fig. S2. Experimental setup and system architecture

Fig. S3. Measurement of laser position repeatability

Fig. S4. Optical component schematic

Movie S1: Principle of operation

Movie S2: Device assembly

Movie S3: Hysteresis compensation

Movie S4: Sigmoid profiling of control inputs

Movie S5: High-speed trajectory following

Movie S6: Complex trajectory following

Movie S7: Multi-modal control

Movie S8: Colonoscope integration and deployment

References

1. R. H. Taylor, "A perspective on medical robotics," *Proceedings of the IEEE*, vol. 94, no. 9, pp. 1652–1664 (2006).
2. J. H. Palep, "Robotic assisted minimally invasive surgery," *Journal of Minimal Access Surgery*, vol. 5, no. 1, pp. 1-7 (2009).
3. P. J. Swaney, P. A. York, H. B. Gilbert, J. Burgner-Kahrs, and R. J. Webster, "Design, fabrication, and testing of a needle-sized wrist for surgical instruments," *Journal of Medical Devices*, vol. 11, no. 1, p. 014501 (2017).
4. J. Kim, W. Lee, S. Kang, K.-J. Cho, and C. Kim, "A needlescopic wrist mechanism with articulated motion and kinematic tractability for micro laparoscopic surgery," *IEEE/ASME Transactions on Mechatronics*, vol. 25, no. 1, pp.229-238 (2019).
5. K. Chandrasekaran and A. Thondiyath, "Design of a tether-driven minimally invasive robotic surgical tool with decoupled degree-of-freedom wrist," *The International Journal of Medical Robotics and Computer Assisted Surgery*, vol. 16, no. 3, p. e2084 (2020).
6. G. Sankaranarayanan, R. R. Resapu, D. B. Jones, S. Schwaitzberg, and S. De, "Common uses and cited complications of energy in surgery," *Surgical Endoscopy*, vol. 27, no. 9, pp. 3056–3072 (2013).
7. P. Kronenberg and O. Traxer, "Update on lasers in urology 2014: current assessment on holmium: yttrium–aluminum–garnet (Ho: Yag) laser lithotripter settings and laser fibers," *World Journal of Urology*, vol. 33, no. 4, pp. 463–469 (2015).
8. G. E. Tontini, H. Neumann, A. Rimondi, S. Vavassori, B. Bruni, G. Cattignoli, P.-H. Zhou, L. Pastorelli, and M. Vecchi, "Ex vivo experimental study on the thulium laser system: new horizons for interventional endoscopy," *Endoscopy International Open*, vol. 5, no. 06, pp. E410–E415 (2017).
9. M. Karaman, T. Gün, B. Temelkuran, E. Aynacı, C. Kaya, and A. M. Tekin, "Comparison of fiber delivered CO2 laser and electrocautery in transoral robot assisted tongue base surgery," *European Archives of Oto-Rhino-Laryngology*, vol. 274, no. 5, pp. 2273–2279 (2017).
10. V. S. Vanni, J. Ottolina, G. Candotti, L. M. Castellano, I. Tandoi, F. S. DE, G. Poppi, S. Ferrari, and M. Candiani, "Flexible CO2 laser fiber: first look at the learning curve required in gynecological laparoscopy training." *Minerva Ginecologica*, vol. 70, no. 1, pp. 53–57 (2018).
11. A. S. Schimberg, T. M. Klabbers, D. J. Wellenstein, F. Heutink, J. Honings, I. van Engen-Van Grunsven, R. M. Verdaasdonk, R. P. Takes, and G. B. Van den Broek, "Optimizing settings for office-based endoscopic CO2 laser surgery using an experimental vocal cord model," *The Laryngoscope*, vol. 10, no. 11, E680-E685 (2020).
12. M. A. Ansari, M. Erfanzadeh, and E. Mohajerani, "Mechanisms of laser-tissue interaction: II. tissue thermal properties," *Journal of Lasers in Medical Sciences*, vol. 4, no. 3, p. 99-106 (2013).
13. A. J. Welch, M. J. Van Gemert et al., *Optical-thermal Response of Laser-irradiated Tissue*. Springer, 2011, vol. 2.

14. M. Remacle, G. Lawson, M.-C. Nollevaux, and M. Delos, "Current state of scanning micromanipulator applications with the carbon dioxide laser," *Annals of Otolaryngology, Rhinology & Laryngology*, vol. 117, no. 4, pp. 239–244 (2008).
15. L. Reinisch and C. G. Garrett, "Laryngeal temperature simulations during carbon dioxide laser irradiation delivered by a scanning micromanipulator," *Lasers in Medical Science*, vol. 34, no. 5, pp. 1011–1017 (2019).
16. D. Kundrat, A. Schoob, T. Piskon, R. Grässlin, P. J. Schuler, T. K. Hoffmann, L. A. Kahrs, and T. Ortmaier, "Toward assistive technologies for focus adjustment in teleoperated robotic non-contact laser surgery," *IEEE Transactions on Medical Robotics and Bionics*, vol. 1, no. 3, pp. 145–157 (2019).
17. D. Kundrat, R. Graesslin, A. Schoob, D. Friedrich, M. Scheithauer, T. Hoffmann, T. Ortmaier, L. Kahrs, and P. Schuler, "Preclinical performance evaluation of a robotic endoscope for non-contact laser surgery," *Annals of Biomedical Engineering* (2020).
18. M. Zhao, T. J. O. Vrieland, A. A. Kogkas, M. S. Runciman, D. S. Elson, and G. P. Mylonas, "LaryngoTORS: A novel cable-driven parallel robotic system for transoral laser phonosurgery," *IEEE Robotics and Automation Letters*, vol. 5, no. 2, pp. 1516–1523 (2020).
19. A. Acemoglu, D. Pucci, and L. S. Mattos, "Design and control of a magnetic laser scanner for endoscopic microsurgies," *IEEE/ASME Transactions on Mechatronics*, vol. 24, no. 2, pp. 527–537 (2019).
20. K. Rabenoroso, B. Tasca, A. Zerbib, P. Rougeot, N. Andreff, and T. E. Pengwang, "Squipabot: A mesoscale parallel robot for a laser phonosurgery," *International Journal of Optomechatronics*, vol. 9, no. 4, pp. 310–324 (2015).
21. R. Renevier, B. Tamadazte, K. Rabenoroso, L. Tavernier, and N. Andreff, "Endoscopic laser surgery: design, modeling and control," *IEEE/ASME Transactions on Mechatronics*, vol. 22, no. 1, pp. 99–106 (2017).
22. S. Patel, M. Rajadhyaksha, S. Kirov, Y. Li, and R. Toledo-Crow, "Endoscopic laser scalpel for head and neck cancer surgery," in *Photonic Therapeutics and Diagnostics VIII, International Society for Optics and Photonics*, p. 82071S (2012).
23. S. A. Bothner, P. A. York, P. C. Song, and R. J. Wood, "A compact laser-steering end-effector for transoral robotic surgery," in *IEEE International Conference on Intelligent Robots and Systems*, pp. 7091–7096 (2019).
24. J. P. Whitney, P. S. Sreetharan, K. Y. Ma, and R. J. Wood, "Pop-up book MEMS," *Journal of Micromechanics and Microengineering*, vol. 21, no. 11, p. 115021 (2011).
25. P. S. Sreetharan, J. P. Whitney, M. D. Strauss, and R. J. Wood, "Monolithic fabrication of millimeter-scale machines," *Journal of Micromechanics and Microengineering*, vol. 22, no. 5, p. 055027 (2012).
26. F. C. Holsinger, J. S. Magnuson, G. S. Weinstein, J. Y. Chan, H. M. Starmer, R. K. Tsang, E. W. Wong, C. H. Rassekh, N. Bedi, S. S. Hong et al., "A next-generation single-port robotic surgical system for transoral robotic surgery: results from prospective nonrandomized clinical trials," *JAMA Otolaryngology–Head & Neck Surgery*, vol. 145, no. 11, pp. 1027–1034 (2019).

27. K. Hwang, Y.-H. Seo, and K.-H. Jeong, "Microscanners for optical endomicroscopic applications," *Micro and Nano Systems Letters*, vol. 5, no. 1, pp. 1–11 (2017).
28. N. T. Jafferis, M. J. Smith, and R. J. Wood, "Design and manufacturing rules for maximizing the performance of polycrystalline piezoelectric bending actuators," *Smart Materials and Structures*, vol. 24, no. 6, p. 065023 (2015).
29. N. T. Jafferis, E. F. Helbling, M. Karpelson, and R. J. Wood, "Untethered flight of an insect- sized flapping-wing microscale aerial vehicle," *Nature*, vol. 570, no. 7762, pp. 491–495 (2019).
30. J. M. Vasantachart, M. Lightfoot, A. Yeo, J. Maldonado, R. Li, M. Alsyouf, J. Martin, M. Lee, G. Olgin, and D. D. Baldwin, "Laser fiber cleaving techniques: effects on tip morphology and power output," *Journal of Endourology*, vol. 29, no. 1, pp. 84–89 (2015).
31. R. Kiesslich, J. Burg, M. Vieth, J. Gnaendiger, M. Enders, P. Delaney, A. Polglase, W. McLaren, D. Janell, S. Thomas et al., "Confocal laser endoscopy for diagnosing intraepithelial neoplasias and colorectal cancer in vivo," *Gastroenterology*, vol. 127, no. 3, pp. 706– 713 (2004).
32. P. R. Rizun and G. R. Sutherland, "Surgical laser augmented with haptic feedback and visible trajectory," in *IEEE Conference on Virtual Reality*, pp. 241–244, (2005).
33. L. Fichera, C. Pacchierotti, E. Olivieri, D. Prattichizzo, and L. S. Mattos, "Kinesthetic and vibrotactile haptic feedback improves the performance of laser microsurgery," in *IEEE Haptics Symposium*, pp. 59–64 (2016).
34. E. Olivieri, G. Barresi, D. G. Caldwell, and L. S. Mattos, "Haptic feedback for control and active constraints in contactless laser surgery: concept, implementation, and evaluation," *IEEE Transactions on Haptics*, vol. 11, no. 2, pp. 241–254, (2017).
35. S. Z. Mansour, R. J. Seethaler, Y. R. Teo, Y. K. Yong, and A. J. Fleming, "Piezoelectric bimorph actuator with integrated strain sensing electrodes," *IEEE Sensors Journal*, vol. 18, no. 14, pp. 5812–5817, (2018).
36. K. Jayaram, N. T. Jafferis, N. Doshi, B. Goldberg, and R. J. Wood, "Concomitant sensing and actuation for piezoelectric microrobots," *Smart Materials and Structures*, vol. 27, no. 6, p. 065028, (2018).
37. J. Puig-Suari, C. Turner, and W. Ahlgren, "Development of the standard cubesat deployer and a cubesat class picosatellite," in *IEEE Aerospace Conference Proceedings* (Cat. No. 01TH8542), vol. 1, pp. 347–353 (2001).
38. T. Mizuno, T. Kase, T. Shiina, M. Mita, N. Namiki, H. Senshu, R. Yamada, H. Noda, H. Kunitani, N. Hirata et al., "Development of the laser altimeter (LIDAR) for Hayabusa2," *Space Science Reviews*, vol. 208, no. 1-4, pp. 33–47 (2017).
39. D. Grassani, E. Tagkoudi, H. Guo, C. Herkommer, F. Yang, T. J. Kippenberg, and C.-S. Brès, "Mid infrared gas spectroscopy using efficient fiber laser driven photonic chip-based supercontinuum," *Nature Communications*, vol. 10, no. 1, pp. 1–8 (2019).
40. H.G. Kim, J. N. Kim, T. W. Na, K. C. Park, and I. K. Oh, "Motion control of piezoelectric tripod platform via feedforward hysteresis compensation," *Advanced Materials Technologies*, vol. 3, no. 12, p. 1800298 (2018).

Acknowledgments: We thank all members of the Harvard Microrobotics Laboratory for their advice and assistance, especially Noah T. Jafferis for his guidance on microrobotic transmission design and Simon Bothner for his contributions to the prior work out of which this research emerged.

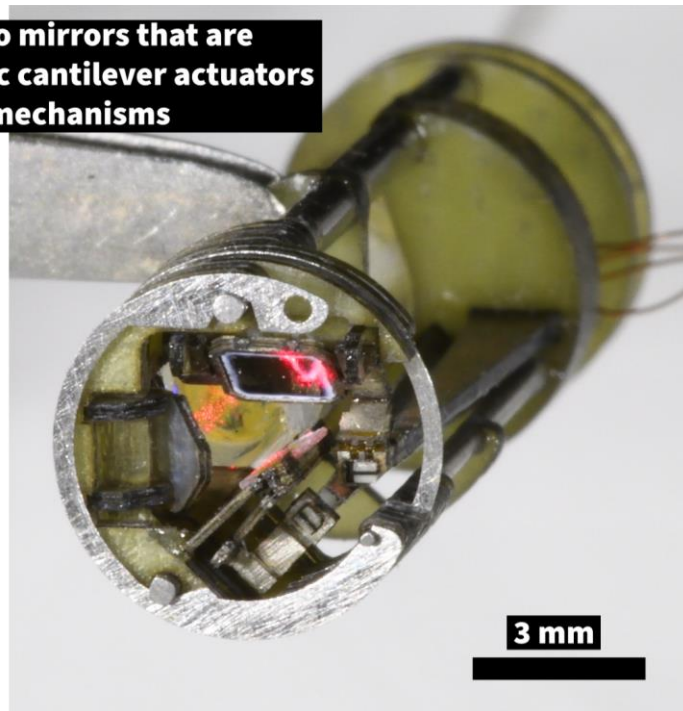
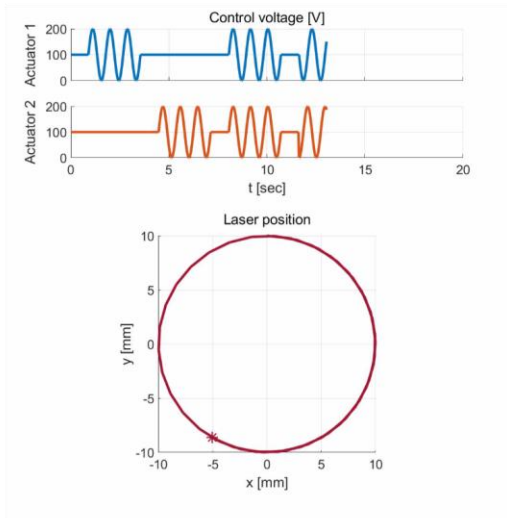
Funding: The authors gratefully acknowledge funding from the National Science Foundation (award #CMMI-1830291) and the Wyss Institute for Biologically Inspired Engineering. Any opinions, findings, and conclusions or recommendations expressed in this material are those of the authors and do not necessarily reflect the views of the National Science Foundation.

Author contributions: P.A.Y, R.P, D.K., and R.J.W initiated and conceptualized the project. P.A.Y. conducted the design, fabrication, and experiments, and R.P. assisted with the colonoscope demonstration. P.A.Y. wrote the original manuscript and R.P, D.K., and R.J.W reviewed and edited the final manuscript.

Competing interests: The authors declare that they have no competing interests.

Data and materials availability: All data needed to evaluate the conclusions are included in the paper or the Supplementary Materials. Please contact P.A.Y. for additional materials and data requests.

The laser position is controlled by two mirrors that are independently driven by piezoelectric cantilever actuators acting through miniature compliant mechanisms



Movie 1. Overview of the microrobotic laser steering system

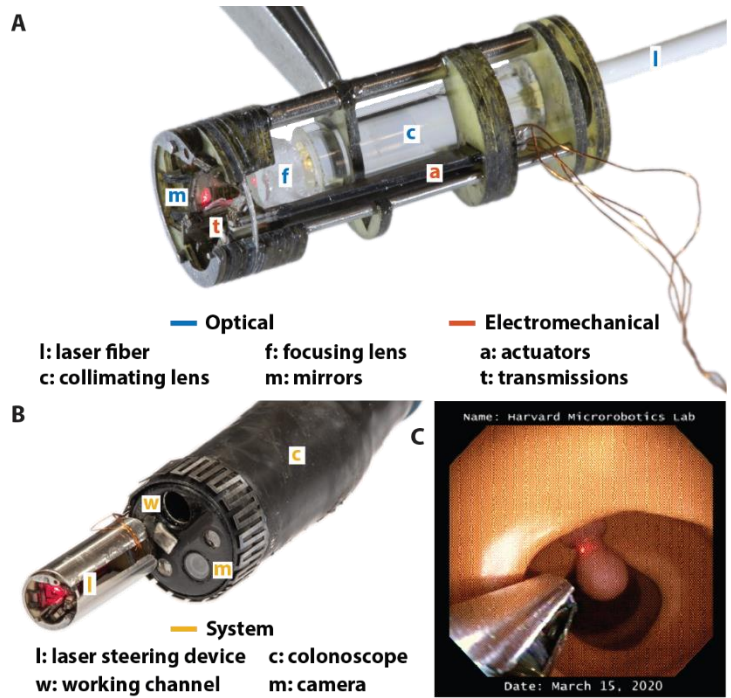


Fig. 1. Microrobotic laser steering device. **A** The 6-mm diameter device receives a fiber-delivered laser, collects the light using a gradient-index collimator, focuses the light using a miniature plano-convex lens, and uses a miniature two-mirror galvanometer to control the angle of the exiting ray. **B** The laser steering device, partially encapsulated and affixed to a colonoscope. Because the device is sufficiently small, it can be integrated with the colonoscope while maintaining standard visualization, illumination, and working channel access. **C** The colonoscope view of a simulated polyp resection procedure. Note that the laser steering tool fills only a small portion of the visual field.

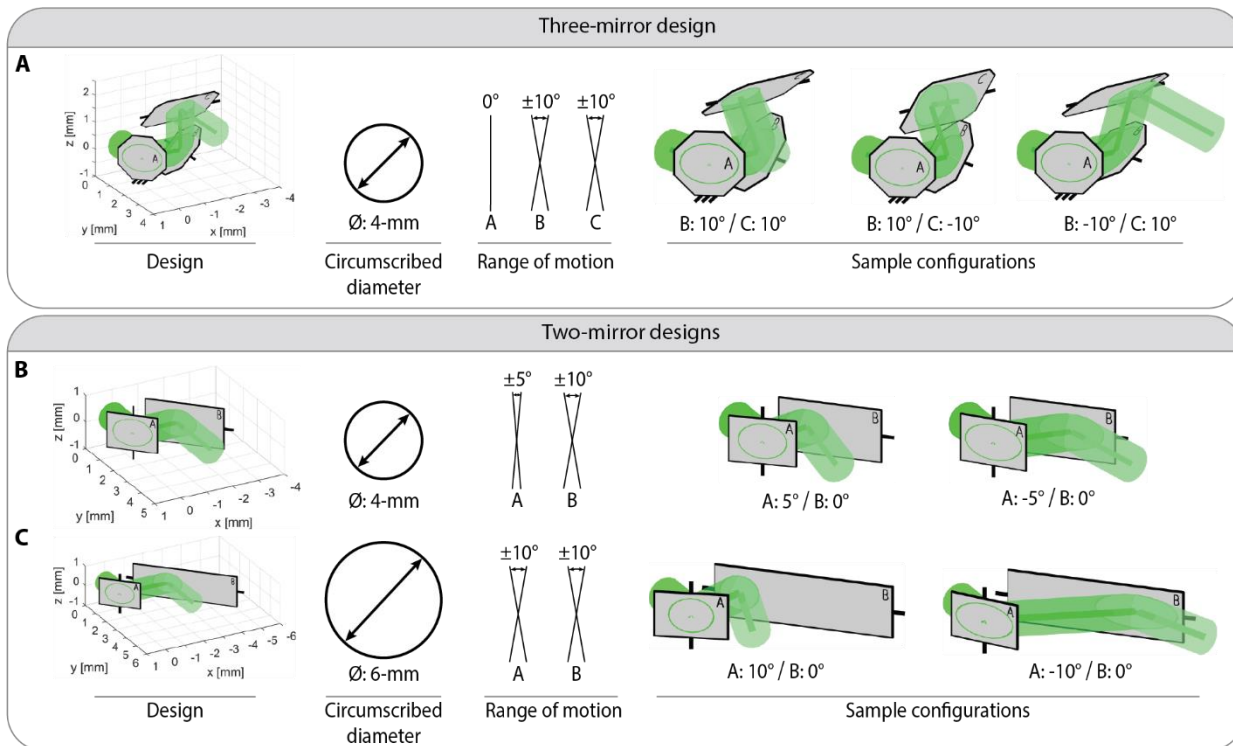


Fig. 2. Design for range of motion and miniaturization. **A** The three-mirror galvanometer achieves a larger range of motion than **B** a two-mirror design of the same size, and a **C** 50% larger diameter two-mirror design is needed to achieve the same range of motion as the three-mirror design. Range of motion is primarily determined by the ability of the mirrors to fully capture and reflect the incident light, but it is limited by the need to avoid collisions between mirrors and collisions between the reflected laser and previous mirrors in the optical path. Sample configurations show the limits of the range of motion at which these collisions are about to occur.

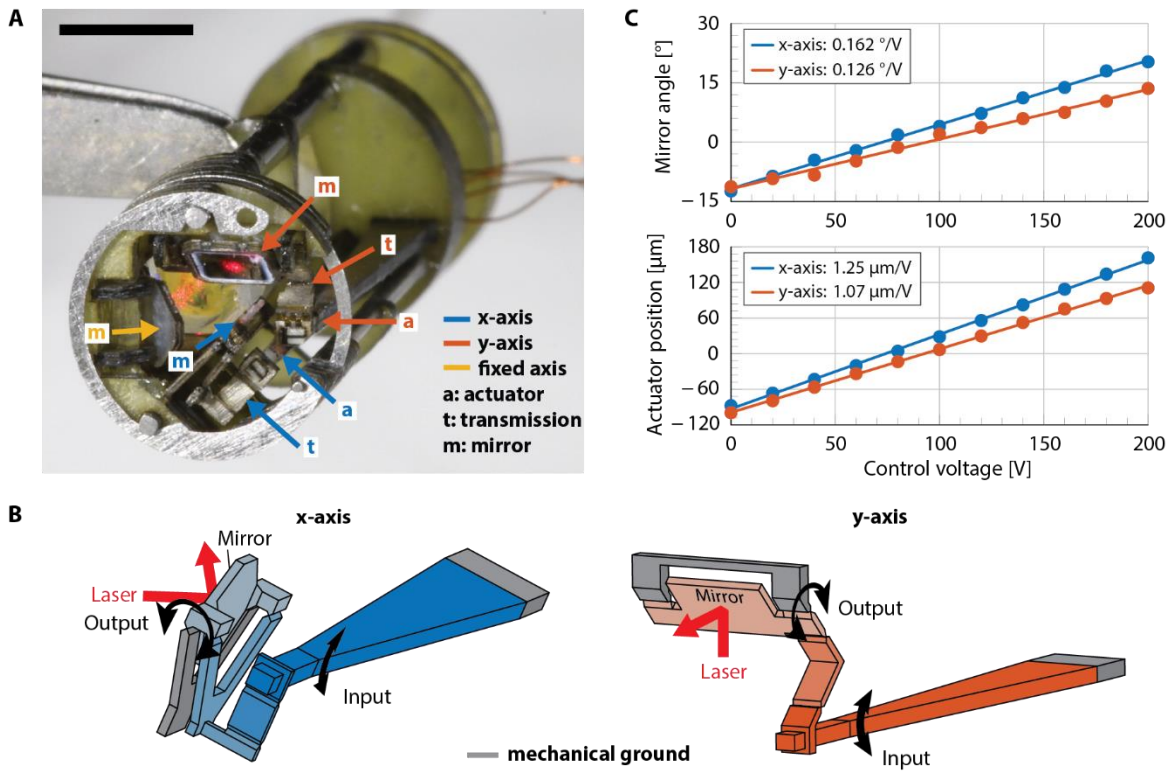


Fig. 3. Device components and kinematic structure. **A** Detailed view of the galvanometer. Piezoelectric bending actuators control the angles of the mirrors via compact motion transmissions made from compliant polyimide joints and rigid stainless steel links. The scale bar is 3 mm. **B** Kinematic structure of the two motion transmissions, which convert the quasi-linear (parabolic) input motion into rotational motion of the mirrors. They are shown in roughly the same orientation as in the above image. **C** Measured linkage kinematics showing the nominal relationships between control voltage, actuator position, and mirror angle. These relationships are not used directly for control; rather, they validate the designed linkage stiffnesses and transmission ratios.
























Device components	Retaining clip	Fixed mirror	Y-axis mirror	X-axis mirror	Focusing lens	Piezoelectric actuators	Collimating lens	Superstructure
Methods of Fabrication								
UV Laser								
Precision lamination								
Sputter deposition								
Off the shelf					OTS		OTS	
Diamond grinding								

Fig. 4. Device components and fabrication. The key components of the laser steering device are shown in assembly order from the superstructure to the retaining clip. The icons below each component show the methods of fabrication used.

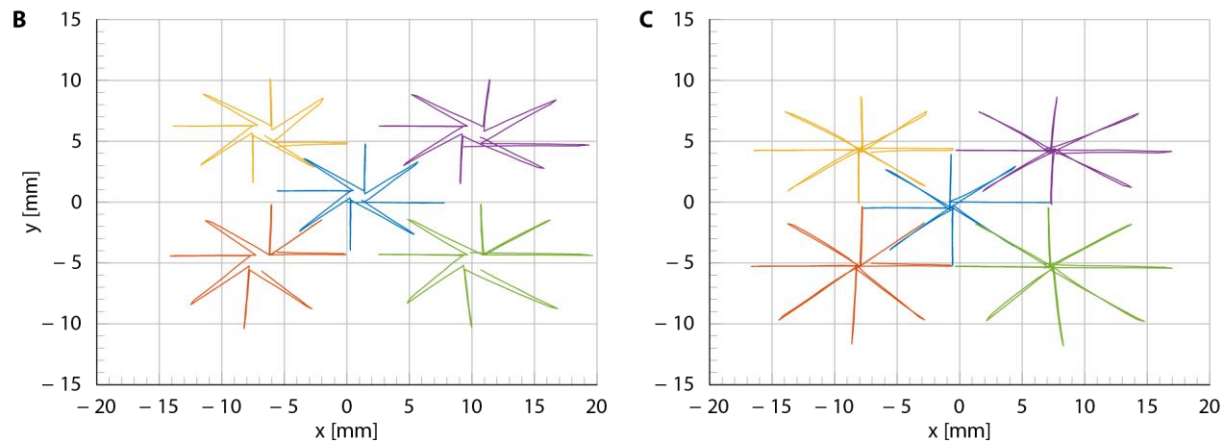
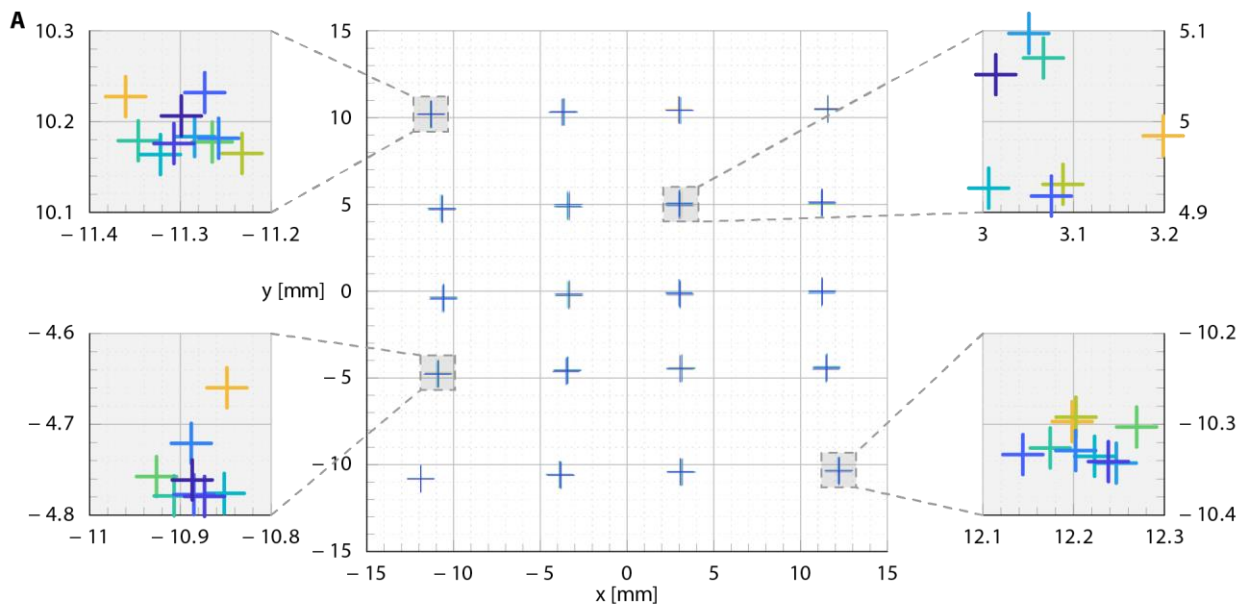


Fig. 5. Laser position control. **A** Laser position repeatability measurements with detail shown in zoomed-in plots. **B** Setpoint regulation without hysteresis compensation and **C** with compensation for the hysteresis arising from domain reorientation within the piezoelectric actuators. Color represents individual trials.

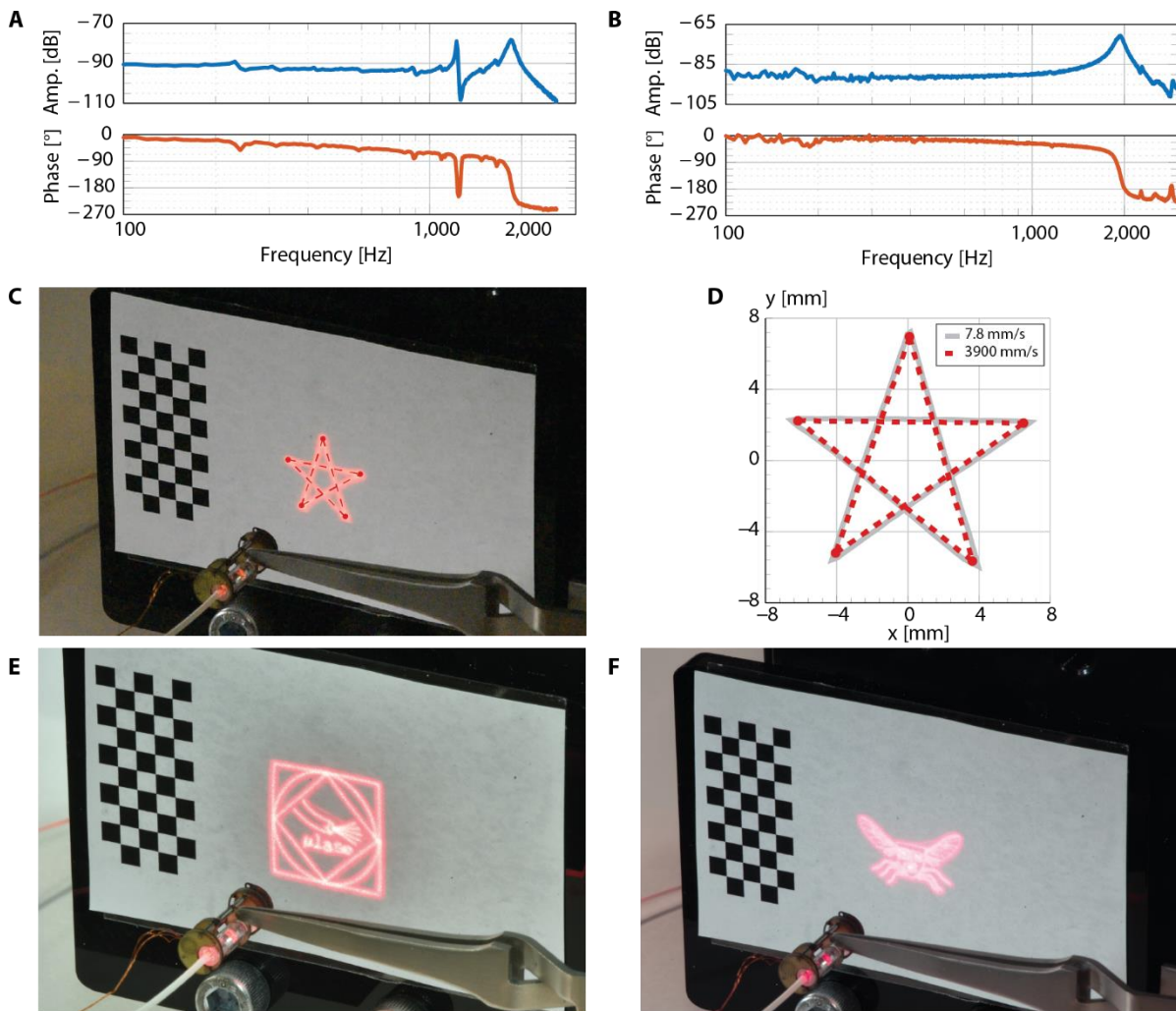


Fig. 6. High-speed control. **A** First mirror (x-axis) frequency response to low-voltage white noise input. **B** Second mirror (y-axis) frequency response. **C** An image created by high-speed motion of the laser steering system. **D** The high-speed image closely matches the trajectory followed by the laser system at low speeds. There is only 5% deviation between the two trajectories, despite a difference in speed of $500\times$. **E-F** Complex images captured through long-exposure photography that demonstrate the system's intricate control capabilities.

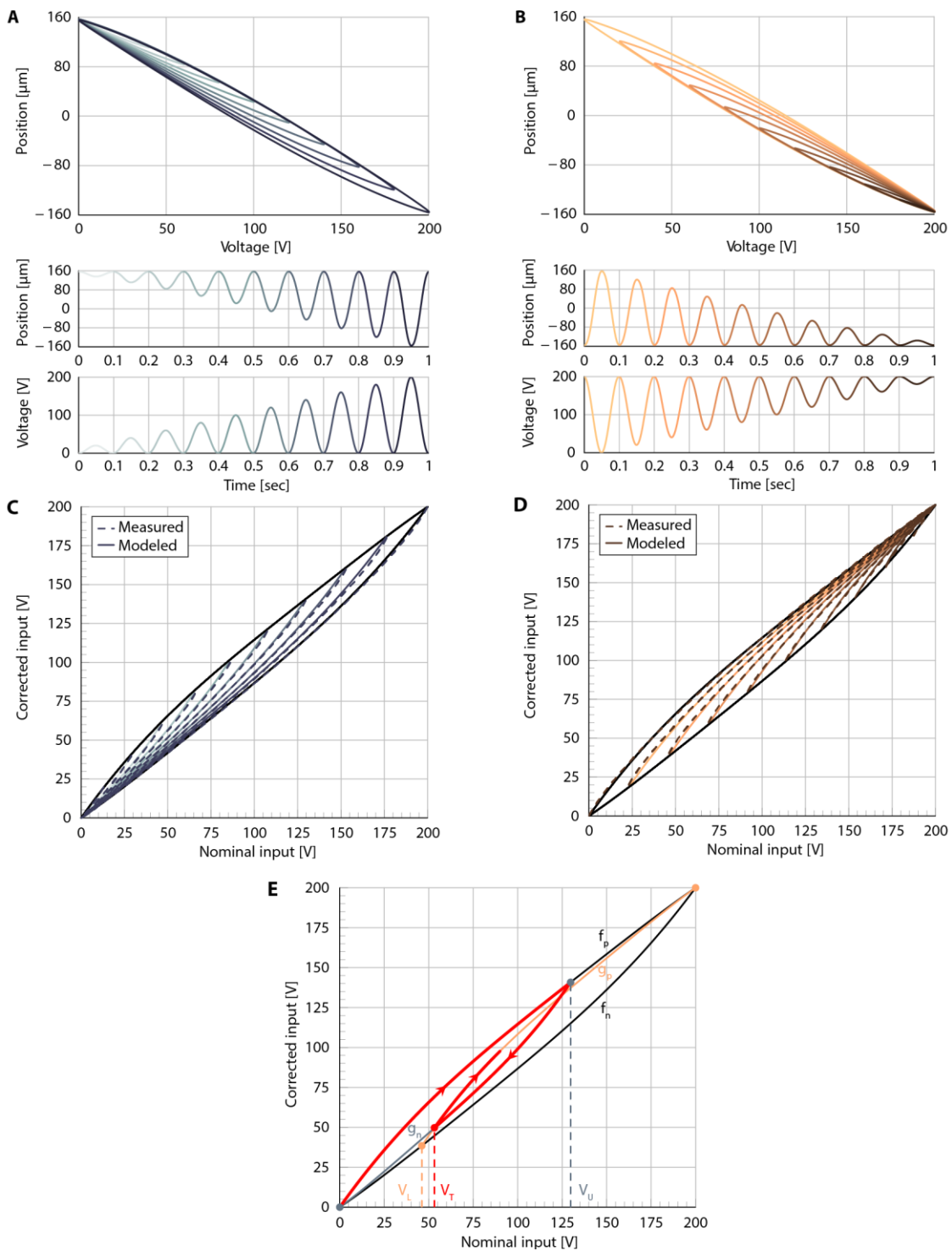


Fig. 7. Hysteresis measurement and modeling. **A-B** Amplitude rich voltage inputs yield the hysteresis curves that are shown. These curves are scaled and inverted to yield the solid curves shown in **C-D**, which are plotted together with the fitted model behavior. **E** Hysteresis model with key functions and parameters shown. The outer envelope is defined by the curves f_p and f_n , and the inner family of curves are defined by g_p and g_n . The subscript denotes the sign of the input rate (positive or negative). The sample trajectory shown in red shows the process of calculating the corrected input for a given nominal input.

	Fiber steering			Optical steering			
	Kundrat (16, 17)	Zhao (18)	Acemoglu (19)	Andreff (20, 21)	Patel (22)	Bothner (23)	This work
Diameter [mm]	11.5	22	13	14	17	15	6
Length [mm]	45*	22	60	42	50	45	16
Working distance [mm]	20	1	30	20	25‡	20	25
Range of motion [mm]	45 × 45	28 ∅	4 × 4	20 × 20	26.5 ∅	18 × 10	18 × 18
Maximum speed [mm/s]	3.5	3	94	33†	167†	2000	3900
Mechanical Bandwidth [Hz]	-	-	63	270	-	750	1200

Table 1. Comparison to state of the art. Our microrobotic approach to laser steering allows miniaturization beyond what was previously achievable. We also achieve higher dynamic performance while maintaining a similar range of motion to existing devices. The device described in (23) was preliminary to the work described herein. *Approximation based on published images. † Calculated from published data. ‡ Patel, et al., tested their device at a long working distance (373 mm), which yielded a diametral range of motion of 396 mm. To facilitate comparison with the other state of the art devices, we show their expected performance with a focal length suitable for the minimally invasive surgical application (25 mm).

Supplementary Materials

Additional considerations for miniaturization

There are several additional considerations for miniaturization that should be taken into account when integrating this device with a specific surgical laser. In particular, there are tradeoffs between device length, width, stand-off distance, and laser spot size. These can be seen with the assistance of Fig. S4, which schematically represents the collimation and focusing of the fiber-delivered beam. Assuming the use of ideal thin lenses and small angles of refraction, the product of the image size and ray angle is invariant, and terms involving $\sin(\theta)$ can be replaced by θ . Under these assumptions, there is the following simple relation for spot size radius y_4 as a function of collimator focal length f_c , focusing lens focal length f_f , and fiber core radius y_1 :

$$y_4 = \frac{f_f}{f_c} y_1$$

Assuming there is some desired stand-off distance from the device to the surgical site, we see that there is an inverse relationship between spot size and collimator focal length. This means that the device length must be increased in order to reduce the size of the laser spot. For example, if a stand-off distance of 20 mm is desired and one is using a fiber with a 500 μm core, which is typical of flexible CO2 laser fibers, such as the Lumenis FiberLase (Lumenis Ltd., Yokneam, Israel), a 10 mm collimator length would be needed to achieve a 1 mm spot size. Thus, achieving a larger stand-off distance and smaller spot size will have an adverse effect on miniaturization, requiring elongation of the device.

Conversely, the scaling of the device diameter is largely a function of the angle of dispersion of the laser as it exits the fiber, i.e., the fiber's numerical aperture. This follows from the scaling of the radius of the collimated beam y_2 , which can be written as a function of the collimator focal length f_c and the angle of dispersion of the fiber θ_1 :

$$y_2 = f_c \theta_1$$

For a given collimator focal length, collimated beam size scales directly with the fiber's angle of dispersion. Increasing the size of the collimated beam requires the use of larger optical components, which necessitates increasing device diameter. This is especially important when scaling the galvanometer components; based on the analysis in the Design section, we expect that device diameter will scale roughly linearly with collimated beam diameter for a given desired range of motion. This means that if small device diameter is desired, a fiber with suitably low angle of dispersion should be used. For example, if a 1 mm collimated beam diameter is desired, as we assumed in the Design section, with a collimator focal length of 10 mm, a fiber with a dispersion angle of 0.1 rad would be needed. For this scenario, an optical cable such as the PIR 400/500 (Arts Photonics GmbH, Berlin, Germany) with core diameter 400 μm and numerical aperture 0.1 rad could be used.

Figures

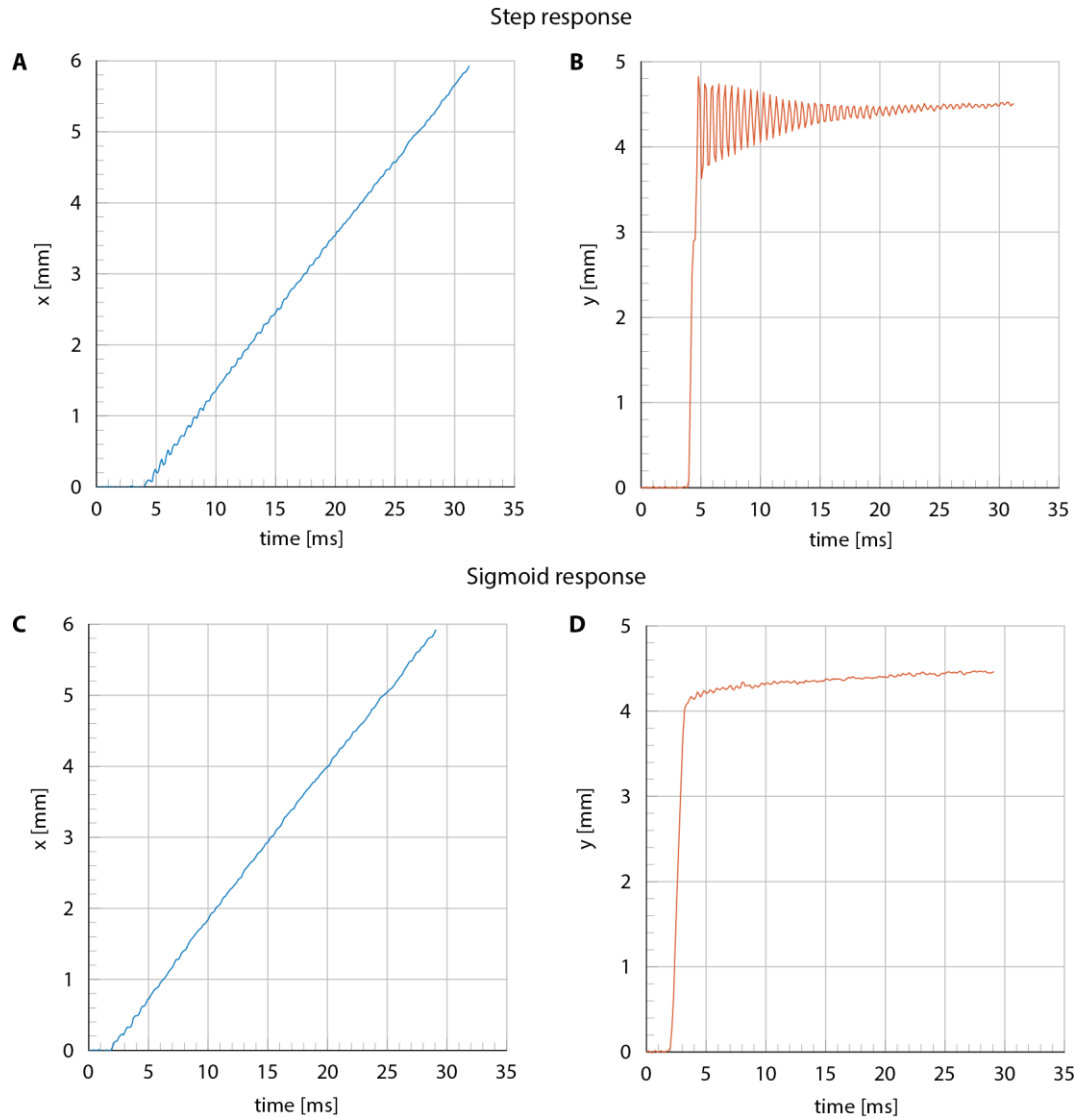


Fig. S1. Time history of step and sigmoid responses. Raw data from Movie S4 showing the laser position of a step response (**AB**) compared to a sigmoid (**CD**) response. The sigmoid input ensures that the motion profile has finite jerk, which prevents the oscillations that can be seen in the step response. The tradeoff is some loss in absolute speed (i.e., rise time): the maximum y component of laser velocity is 5900 mm/s for the step input and 3900 mm/s for the sigmoid input.

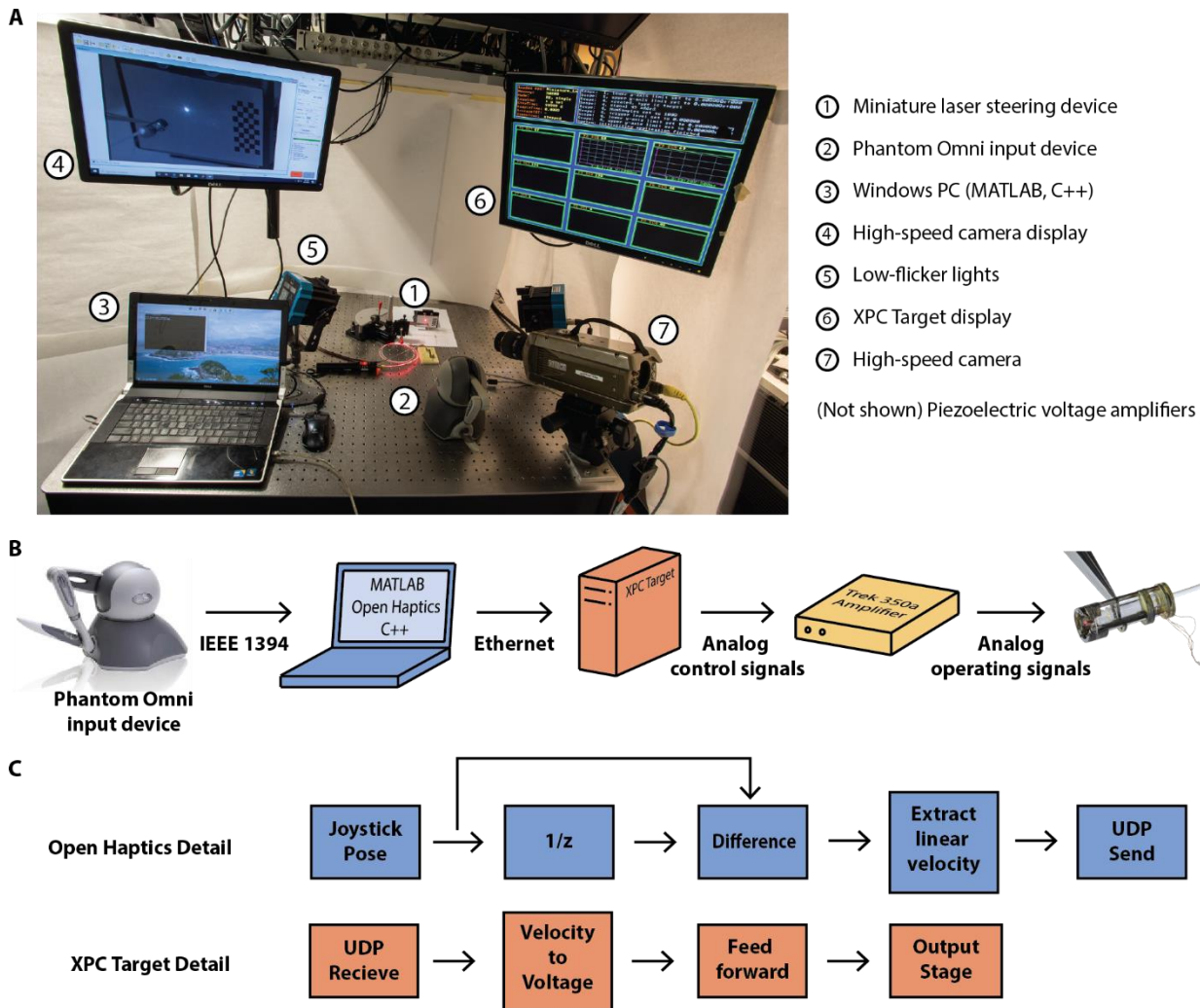


Fig. S2. Experimental setup and system architecture. **A** Measurement setup for collecting laser spot position with high-speed camera, low-flicker lighting, and supporting equipment. **B** Hardware architecture and signal flow for laser teleoperation from the joystick input device to the laser steering tool. **C** Program flow for mapping joystick pose to actuator inputs within the Open Haptics API and XPC Target.

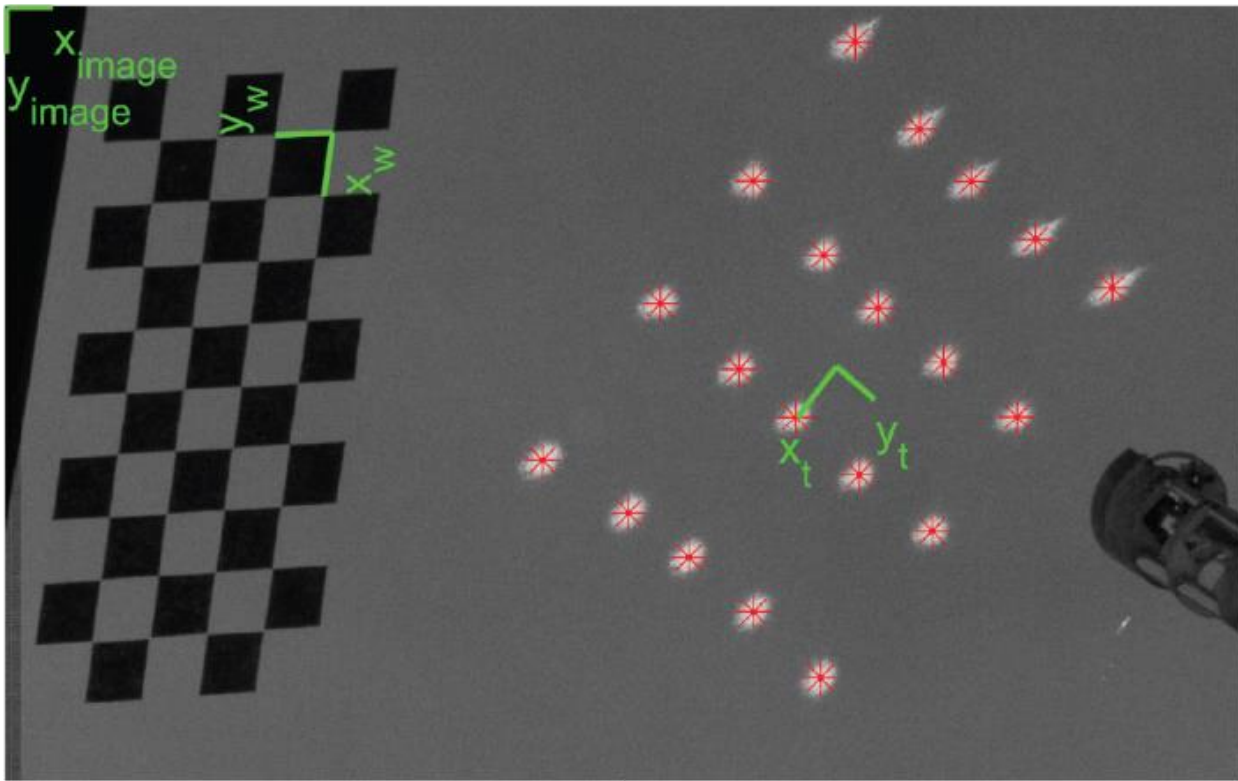


Fig. S3. Measurement of laser position repeatability. This image contains 20 sampled points in the laser workspace superimposed onto a single image. The data for 10 such trials is compiled and shown in Fig. 5A.

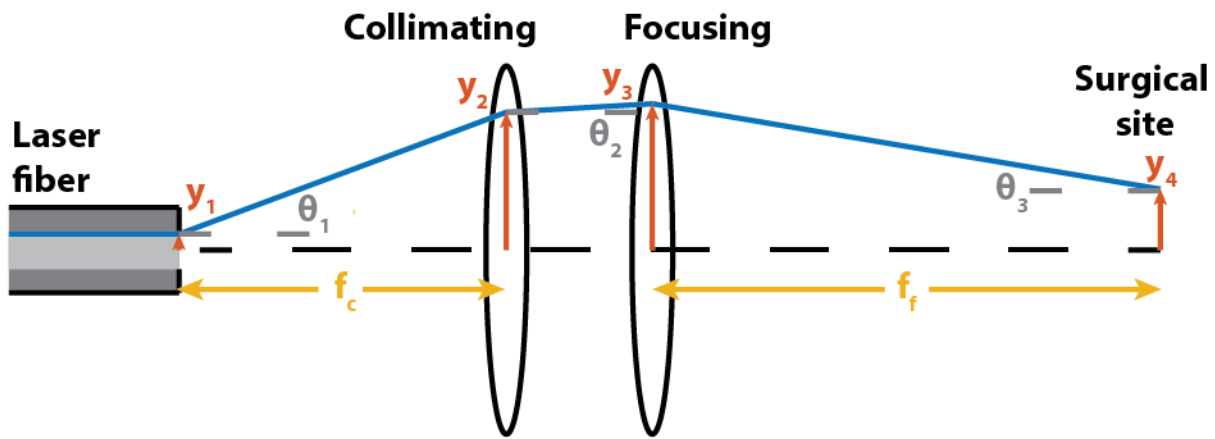


Fig. S4. Optical component schematic. The nominal laser beam size throughout the device is a function of the laser fiber's core size y_1 , dispersion angle θ_1 and the focal lengths f_c and f_f of the collimating and focusing optics.

Videos

Movie S1: Principle of operation. Individual components are highlighted and their contribution to overall device function described. The relationship between input control voltage and output laser position is shown.

Movie S2: Device assembly. Assembly is straightforward due to the modular design and fabrication approach. This video shows zoomed-in detail of the entire assembly process.

Movie S3: Hysteresis compensation. Setpoint regulation with and without hysteresis compensation, which dramatically improves the quality of control.

Movie S4: Sigmoid profiling of control inputs. Using sigmoid input profiles avoids exciting the resonant modes of the mirrors, which is important for high-speed control. The time history of the trajectories is shown in Fig. S1.

Movie S5: High-speed trajectory following. The same star trajectory is traced at low (7.8 mm/s) and high speeds (3900 mm/s). Both the rendered images and the zoomed-in motion of the device are shown.

Movie S6: Complex trajectory following. Using high-speed control the device draws two complex images: a logo of the laser steering tool and the Harvard Microrobotics Lab logo.

Movie S7: Multi-modal control. By leveraging the high bandwidth of the device, high-speed trajectories can be interposed on low-speed ones to allow on-the-fly control over the area of laser application.

Movie S8: Colonoscope integration and deployment. The laser steering device is integrated with a commercial colonoscope (Olympus CF-100L); teleoperated and automated operation are shown.